

Article

Influence of Vertical Force on Shields' Curve and Its Extension in Rapidly Varied Flow

Muhammad Zain Bin Riaz ^{1,*}, Umair Iqbal ², Huda Zain ³, Shu-Qing Yang ¹, Muttucumaru Sivakumar ¹, Rong Ji ¹ and Muhammad Naveed Anjum ⁴

¹ School of Civil, Mining, Environmental and Architectural Engineering (SCMEA), University of Wollongong, Wollongong, NSW 2522, Australia; shuqing@uow.edu.au (S.-Q.Y.)

² University of Newcastle, Newcastle, NSW 2308, Australia

³ Department of Chemical Engineering, Faculty of Chemical, Metallurgical & Polymer Engineering, University of Engineering and Technology, Lahore 54890, Pakistan

⁴ Department of Land and Water Conservation Engineering, Faculty of Agricultural Engineering and Technology, PMAS-Arid Agriculture University, Rawalpindi 46000, Pakistan

* Correspondence: mriaz@uow.edu.au

Abstract: Sediment transport is a geophysical phenomenon characterized by the displacement of sediment particles in both the horizontal and vertical directions due to various forces. Most of the sediment transport equations currently used include only parameters related to the horizontal direction. This study measured both instantaneous longitudinal and vertical parameters, i.e., velocities and forces, and found that the magnitude and direction of the vertical force play an important role in sediment incipient motion. An innovative experimental system was developed to investigate the effect of vertical force on incipient motion in rapidly varying flows. A quadrant analysis of the instantaneous measured forces on the critical shear stress was performed. The research revealed that upward positive vertical forces enhance particle mobility, whereas downward negative vertical forces increase particle stability. Novel equations have been developed to represent the influence of vertical forces on sediment transport. A comprehensive critical Shields stress for sediment transport was proposed, extending the Classic Shields diagram to encompass the incipient motion in highly unsteady flows.



Citation: Riaz, M.Z.B.; Iqbal, U.; Zain, H.; Yang, S.-Q.; Sivakumar, M.; Ji, R.; Anjum, M.N. Influence of Vertical Force on Shields' Curve and Its Extension in Rapidly Varied Flow. *Water* **2024**, *16*, 2960. <https://doi.org/10.3390/w16202960>

Academic Editors: Francois Marin and Nizar Abcha

Received: 3 September 2024

Revised: 10 October 2024

Accepted: 14 October 2024

Published: 17 October 2024



Copyright: © 2024 by the authors. Licensee MDPI, Basel, Switzerland. This article is an open access article distributed under the terms and conditions of the Creative Commons Attribution (CC BY) license (<https://creativecommons.org/licenses/by/4.0/>).

Keywords: critical shear stress; tidal bore; dam-break bore; shields diagram; sediment transport; vertical force

1. Introduction

A comprehensive understanding of the physics underlying fluid–sediment interactions, wave bottom boundary layer dynamics, and their effects on sediment transport is essential for fully comprehending nearshore coastal processes. Numerous sediment-related issues, including water quality monitoring, pollution management, wetland restoration, reservoir maintenance, beach erosion, and stability of coastal areas and infrastructure, are intrinsically linked to the concept of incipient motion [1]. The concept of incipient motion is essential for investigating the evolution of deltas, changes in the seabed, shoreline formation, and the construction of coastal protection infrastructure [2–6].

The critical conditions for triggering sediment movement are generally classified into two approaches: the critical shear stress approach and critical velocity approach. The shear stress method often employs the critical Shields number or well-known Shields curve. This approach was originally developed by Shields [7], who studied the shear forces on a single grain at the point of movement under steady, uniform flow conditions. Nevertheless, its application is frequently extended to non-uniform or unsteady flows, as exemplified by numerical models [8–12] and laboratory data analysis [13–17]. Frank et al. [14] used the bed shear stress to express the conditions of critical sediment motion. Contrary to

the expected behavior based on the Shields parameter, sediment motion has been documented in certain oscillatory flows [18]. Extensive studies have been conducted to explain this phenomenon [19–22], and some studies have provided a possible reason of pressure gradient-induced motion [14,18,23,24], and most of them attribute it to experimental errors and insist that the Shields curve is still valid for expressing incipient sediment motion.

Madsen [24] suggested that breaking and near-breaking waves create horizontal pressure gradients that can induce bulk instability, thereby leading to shoreward sediment transport. Foster et al. [18] experimentally confirmed the role of pressure gradients in initiating sediment motion due to the free-stream velocity gradients in surface gravity waves. Sleath [25] quantified the effects of these horizontal pressure gradients using Sleath parameter S , which balances the inertial and gravitational forces acting on the sediment particles.

Nielsen [26] revised the traditional Shields parameter to include both fluid acceleration and shear stress. This modified Shields parameter proved to be more accurate in predicting the transport of coarse sediments under shoaling waves than the original formulation based solely on shear stress [27]. Terrile et al. [27] also investigated the impact of wavefront acceleration on the initiation of sediment motion and, found that the accelerating flow increases the lift force on particles, making them more likely to move. Their observations showed that gravel particles with a diameter of 10 mm could move under conditions of high flow acceleration, even when the shear stresses were well below the critical Shields threshold.

Conventionally, instantaneous shear stresses and Shields parameters are based on the average free stream velocity, i.e., the Shields parameter is directly proportional to the square of the horizontal velocity, which is a quasi-steady approach. However, Myrhaug et al. [28] observed sediment transport near the seabed and discovered that the maximum sediment concentration occurred at the lowest velocities ($U \approx 0$), whereas the greatest longitudinal velocity consistently corresponded with lower sediment concentrations. Recently, Riaz et al. [29] observed and demonstrated this phenomenon by directly measuring forces in a laboratory flume for a range of tidal waves. They explained that the Shields parameter is not always proportional to the square of the longitudinal velocity component and that sediment transport can occur below the critical Shields parameter because of the reduction in shear stress caused by the vertical force. Evidently, the shear stress approach does not account for parameters that reflect the vertical parameters, such as the vertical pressure force or lift force induced by the sudden impact of bores. Many researchers ascribe the limited range of applicability of the Shields diagram to complex flows subject to vertical parameters, such as [16,17,29–33]. Additionally, incipient motion caused by vertical parameters may explain the variability observed in the Shields diagram and inconsistencies in Shields values at the onset of sediment movement [29,32,34] in conjunction with horizontal pressure gradients [18,23]. Additionally, it is well-established that vertical pressure gradients play a crucial role in destabilizing the bed [35,36].

In wave-dominated environments, the vertical pressure gradient primarily results from changes in water depth. However, how sudden shifts in water depth affect shear stress remains a topic that requires further investigation [31]. The non-hydrostatic pressure generated by the bores at the water surface can induce uplift forces. Various researchers have proposed modifications to the Shields number and have explored the factors affecting the buoyancy force in fluid dynamics. Francalanci et al. [30] introduced the concept of “apparent density of the fluid”, while Yang [32] put forth the idea of “apparent density of the sediment particle” to adjust the Shields number. In a related study, ref. [37] suggested that non-hydrostatic pressure could influence both the direction and strength of the buoyancy force. Moreover, previous studies on wave conditions have utilized average lift forces [38,39].

In the literature, no study used instantaneous lift and drag force to verify these assumptions in unsteady flows; however, refs. [40–42] showed the importance of instantaneous forces during steady flow. Substantial research efforts have been directed toward examining the impact of tsunamis and dam-break waves on structures in coastal areas and idealized settings [43–46]. Numerous investigations have employed both experimental and numeri-

cal methods to study alterations in bed morphology resulting from dam-break waves over granular surfaces [47–50]. In a recent investigation, Xu et al. [51] utilized a shear plate to quantify the bed shear stresses near the front edge of dam-break waves propagating across a rough surface.

To the best of our knowledge, no prior research has investigated instantaneous three-dimensional hydrodynamic forces to explain the fundamental assumptions and mechanisms of sediment incipient motion during dam-break or tsunami bores. Previous studies have primarily focused on characterizing incipient motion through measurements of the flow velocity, bed evolution, and horizontal pressure gradients. A more comprehensive in situ investigation is necessary to obtain a complete understanding of the actual phenomena of incipient motion as the wavefront breaks.

To comprehensively examine the limited applicability of the Shields curve for predicting sediment initiation, additional laboratory experiments were conducted in rapidly varying flows. This investigation quantitatively elucidates the influence of instantaneous changes in the vertical force on the Shields number and explicates the occasional failure of the Shields curve to accurately estimate the critical shear stress. To address this issue, novel equations have been developed and validated using both direct force measurements and published data. These new formulations are expected to enhance future models of sediment transport for large-scale coastal phenomena.

2. Theoretical Consideration

Sediment transport is influenced by longitudinal and vertical water forces on particles. Researchers have aimed to improve sediment transport models, addressing phase lag and bedform challenges. Francalanci et al. [30] highlighted pressure fluctuations as a major issue, suggesting the incorporation of pressure variations through apparent fluid density. Yang [32,52] introduced sediment apparent density based on the parameter $Y (=V/\omega)$. Potential factors for characterizing the vertical driving force include pressure (P) [30], vertical velocity (V) [52], vertical hydraulic gradient (i) [53], and lift force [16,17,29]. It is evident that all sediment transport equations become invalid when a particle experiences significant vertical motion [32]. Francalanci et al. [30] elucidated this combined effect by reformulating the definition of the dimensionless Shields shear number as the ratio of forces in the longitudinal and vertical directions, as follows:

$$\tau_{*(0)} = \frac{4}{3} \frac{\tau_{c(0)} \frac{1}{2} \pi \left(\frac{d}{2}\right)^2}{\frac{4}{3} (\rho_s - \rho) g \pi \left(\frac{d}{2}\right)^3} = \frac{\tau_{c(0)}}{(\rho_s - \rho) g d} \quad (1)$$

where $\tau_{c(0)}$ = critical shear stress, d = particle diameter, ρ_s and ρ are particle and fluid densities, respectively. They argued that the numerator denotes the longitudinal friction force, and the denominator represents the vertical force, i.e., the effective submerged force of the particle.

In this study, a simpler model, as illustrated in Figure 1, was used, similar to Francalanci et al.'s [30] approach. Here, the instantaneous vertical force (F_v) induced by waves is chosen to represent vertical motion instead of the pressure gradient force. This choice is made because the vertical force is more straightforward and convenient compared to other parameters, such as the pressure gradient force or hydraulic gradient in the sediment layer. The model depicts a permeable bed composed of uniform spherical particles of diameter d . In quantity, the value of the average vertical force $\overline{F_v}$ in steady and uniform flows is much less than shear force, but it may be significant and plays an important role for sediment transport in non-uniform and unsteady flows because it alters the submerged force [54], and flow resistance [29]. In addition, its impact on mass transport needs to be clearly defined.

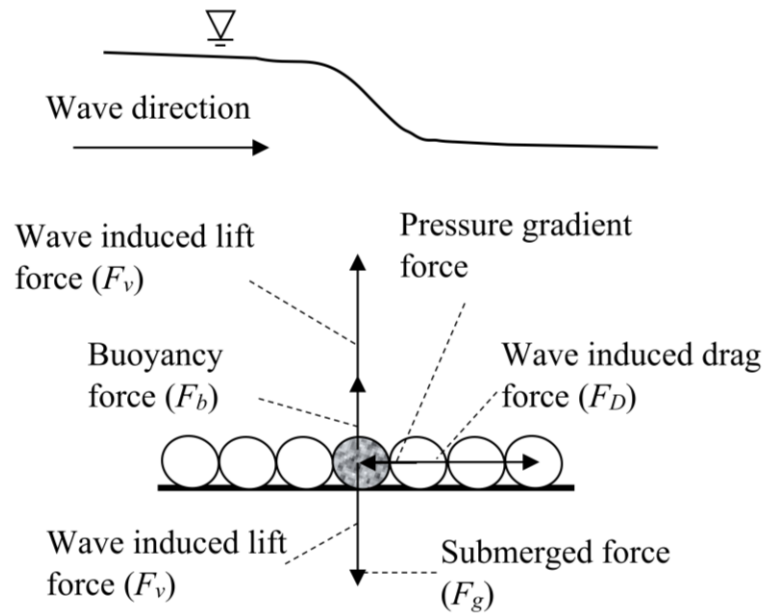


Figure 1. Schematic of longitudinal and vertical forces during wave conditions.

Consider, for example, a spherical particle of diameter “ d ” shown in Figure 1. The origin of the term $(\rho_s - \rho)$ in Equation (1) is the assumption that the downward gravitational force F_g corresponding to the weight of an immersed particle, given as

$$F_g = \rho_s g \frac{4}{3} \pi \left(\frac{d}{2}\right)^3 \tag{2}$$

is partially counterbalanced by the buoyant force F_b corresponding to the weight of the displaced fluid, given as

$$F_b = \rho g \frac{4}{3} \pi \left(\frac{d}{2}\right)^3 \tag{3}$$

So that the effective submerged force F_s of the particle is given as

$$F_s = F_g - F_b = (\rho_s - \rho) g \pi \frac{d^3}{6} \tag{4}$$

The term above appears specifically in the denominator of Equation (1), in which the most important and questionable assumption is that the vertical force F_s is constant and independent of sudden changes in the water surface and unsteadiness owing to unsteady flow. A special experiment is required to test whether this assumption is correct.

In an environment wherein the motion of the surrounding fluid can generate an upward force of lift F_v , the net effective submerged force becomes $F_s - F_v$, where F_s is the effective submerged force and F_v is the instantaneous vertical force. This variation was directly measured. From a mathematical perspective, the reduction in the effective force experienced during submersion can be accounted for by modifying the density from ρ_s to ρ'_s , provided that the particle size remains constant. The equation for the submerged force can subsequently be expressed in a format analogous to Equation (4) as follows:

$$F_{ns} = (\rho'_s - \rho) g \pi \frac{d^3}{6} - F_v \tag{5}$$

alternatively,

$$F_{ns} = (\rho'_s - \rho) g \pi \frac{d^3}{6} \tag{6}$$

where F_v is the vertical force induced by unsteady flows, F_{ns} is the net submerged force in a moving fluid. From Equations (5) and (6), one can derive the following relationship

$$\frac{\rho'_s - \rho}{\rho_s - \rho} = \frac{F_s + F_v}{F_s} \quad (7)$$

or

$$\frac{\rho'_s - \rho}{\rho_s - \rho} = 1 + \frac{F_v}{F_s} \quad (8)$$

In contrast to Francalanci et al.'s [30] approach, which modified fluid density to account for pressure effects, Equation (8) introduces the concept of "apparent particle density" ρ'_s . This equation suggests that the impact of non-hydrostatic pressure can be represented by changes in the sediment density [32]. According to Equation (8), if an upward vertical force ($F_v > 0$) is present, ρ'_s will be less than ρ_s , making the sediment behave like a lighter material. Conversely, if a downward vertical force ($F_v < 0$) is applied, ρ'_s increases, indicating that the sediment behaves more like a heavier material. Thus, Equation (8) shows that an upward vertical force enhances particle mobility by making them "lighter", while a downward vertical force increases particle stability by making them "heavier".

Critical Shear Stress Subject to F_v

It would be interesting to explore how waves influence the onset of sediment movement. For unsteady flows, the traditional Shields diagram may have limited applicability in expressing the threshold for sediment motion [32], due to the presence of vertical forces induced by waves. When the apparent sediment density is incorporated into the Shields number, it takes the following form:

$$\tau'_{*(Y)} = \frac{\tau'_{c(Y)}}{(\rho'_s - \rho)gd} \quad (9)$$

where $\tau'_{c(Y)}$ is the critical shear stress with effect of vertical force. Comparing Equation (9) with Equation (1), one may find that in conventional sediment transport theory, it is impossible to have a zero denominator, but Equation (9) shows that the denominator is a variable and possibly zero.

Equation (9) predicts that, with the Shields number held constant, the critical shear stress observed in a flow with an upward vertical force (F_v) should be lower compared to that in steady and uniform flows. Conversely, a downward vertical force (F_v) requires a higher shear stress to initiate the particle movement. This is because, while the Shields number remains unchanged with the addition of vertical force (F_v), the only variable affecting the particle motion is the required critical shear stress. This can be observed by inserting Equation (7) into Equation (9):

$$\tau'_{*(Y)} = \frac{\tau'_{c(Y)}}{(\rho_s - \rho)gd} \left(\frac{F_s}{F_s - F_v} \right) = \frac{\tau_{c(0)}}{(\rho_s - \rho)gd} \quad (10)$$

If the cases with and without including vertical force are compared, the critical shear stress $\tau_{c(0)}$ and $\tau'_{c(Y)}$ have the following relationship:

$$\frac{\tau'_{c(Y)}}{\tau_{c(0)}} = \left(1 - \frac{F_v}{F_s} \right) \quad (11)$$

Using Equation (1), (10) and (11) can be rewritten as follows:

$$\frac{\tau'_{c(Y)}}{(\rho_s - \rho)gd(1 - F)} = \frac{\tau_{c(0)}}{(\rho_s - \rho)gd} \quad (12)$$

or

$$\frac{\tau'_{c(Y)}}{\tau_{c(0)}} = 1 - F \quad (13)$$

where $F = \frac{F_v}{F_s}$.

Equation (9) incorporates the impact of the vertical force, illustrating that an upward vertical force decreases the apparent density of the particles, which, in turn, lowers the critical shear stress required for sediment movement. Conversely, a downward vertical force increases the apparent density, thereby increasing the required critical shear stress. Equations (10) and (12) describe the relationship between the modified Shields number $\tau'_{*(Y)}$ and the original Shields number $\tau_{*(0)}$. These equations suggest that the presence of a vertical force F_v can cause the original Shields number to significantly deviate from the predicted Shields curve.

3. Experimental Setup and Method

The investigation was conducted in a large glass-walled recirculating flume situated at the University of Wollongong's School of Civil, Mining, Environmental, and Architectural Engineering (SCMEA) in Australia. Riaz et al. [29] provided a comprehensive description of the methodology. This section briefly outlines the experimental setup and protocol. All experiments were performed in a flume with dimensions of 10.5 m in length, 0.4 m in depth, and 0.3 m in width. A pump with a capacity of up to 50 L per second propelled the flow within the flume, connected to a head tank measuring 2.5 m long, 1.8 m deep, and 2 m wide. The flume was equipped with two gates to produce various types of tidal and dam-break bores. Dam-break bores were generated by rapidly opening the sliding sluice gate at the main channel inlet ($x = 0$ m), resulting in an almost instantaneous release of water. Furthermore, a fast-closing, fully obstructing Tainter gate was installed downstream of the channel (at $x = 10$ m). Tidal bores were created by rapidly closing the downstream Tainter gate, with gate openings ranging from 0 to 120 mm, progressing from the downstream end towards the upstream inlet.

For stable flow conditions, water level measurements were obtained utilizing pointer gauges mounted on rails. In the case of unstable flows, two Microsonic™ Mic + 25/IU/TC ultrasonic displacement meters (UDMs) were positioned above the channel to monitor water depths. The UDMs were calibrated under steady flow conditions using pointer gauges, achieving an accuracy of $\pm 1\%$ with built-in temperature drift compensation. The experimental apparatus was designed to operate under hydraulically rough flow conditions ($R_{k*} > 3 \times 10^2$) using $R_{k*} = k_s u_* / \nu$ assuming $k_s = D$, where D is the particle diameter and flows with $R_{k*} \geq 70$ are classified as hydraulically rough [55]. Details of tidal bores with varying Froude numbers (calculated using, $Fr = (V_0 + U_x) / \sqrt{gh_0}$) are provided in Table 1.

Table 1. Experimental flow condition during tidal bore propagation.

Q (m ³ /s)	Gate Opening (mm)	h_0 (m)	Fr
0.04	0, 10, 20, 40 & 60	0.155	1.17–1.45
0.033	0, 10, 20, 40 & 60	0.140	1.17–1.45
0.026	0, 10, 20, 40 & 60	0.125	1.17–1.45

Notes: h_0 ; initial flow depth, Fr ; bore Froude number, Q ; initial flow discharge.

For the dam-break experiments, the reservoir tank was filled to various depths ranging from 250 to 400 mm, with increments of 50 mm. The sliding sluice gate was positioned at either 200 mm or fully open (400 mm). To determine the propagation speed of the dam-break bore tip, U_x , researchers have employed the time-of-flight technique. This method involved calculating the time required for the bore to traverse the distance between two ultrasonic displacement meters (UDM1 and UDM2) and dividing the distance between these meters by that time. This approach, which was previously utilized by [51,56] to

estimate tsunami bore front velocity, was implemented in this investigation. The Froude number of the dam-break bore is defined as $Fr_d = \frac{U_x}{\sqrt{gh_d}}$, where h_d is the maximum dam-break bore depth at the test location. In the experiments, dam-break bore velocities varied from 1.33 to 2.05 m/s, and Fr_d values ranged from 1.4 to 1.7. Table 2 provides detailed information on the dam-break bores. For further details on the bed configurations and their effects, see [29].

Table 2. Experimental flow condition during dam-break bore propagation.

Case	WL (mm)	GO (mm)	U_x (m/s)	Fr_d
1	250	400	1.32	1.40
2	300	400	1.49	1.51
3	350	200	1.65	1.57
4	350	400	1.78	1.62
5	400	200	1.94	1.67
6	400	400	2.06	1.71

Notes: WL; reservoir water level, GO; sluice gate opening.

A waterproof three-axis force sensor was positioned 6 m from the upstream inlet of the channel (Figure 2) to measure the load on the metal foil strain gauges. The sensor’s signals were transmitted via cable to an external amplifier and signal processing system, where they were amplified and converted into force measurements. The apparatus exhibited a sensitivity of 0.88 mN in both the downstream (x) and upward (z) directions, with the latter perpendicular to the flume bed. The cross-axis interference between the x and z axes is negligible, with less than 0.5% and 1% of full scale, respectively. Throughout all experiments, the force sensor operated at a 200 Hz frequency to acquire data.

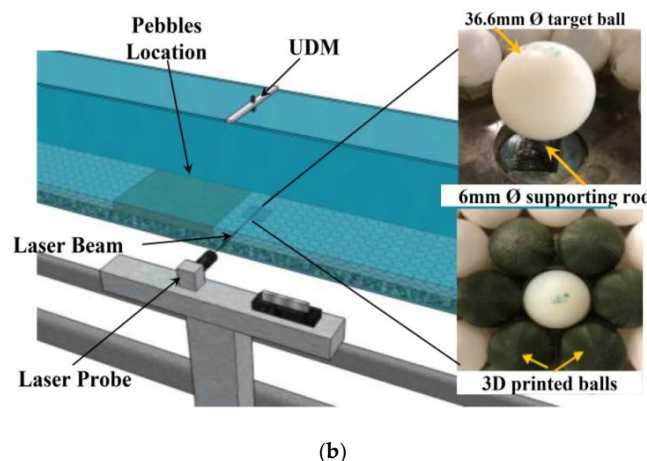
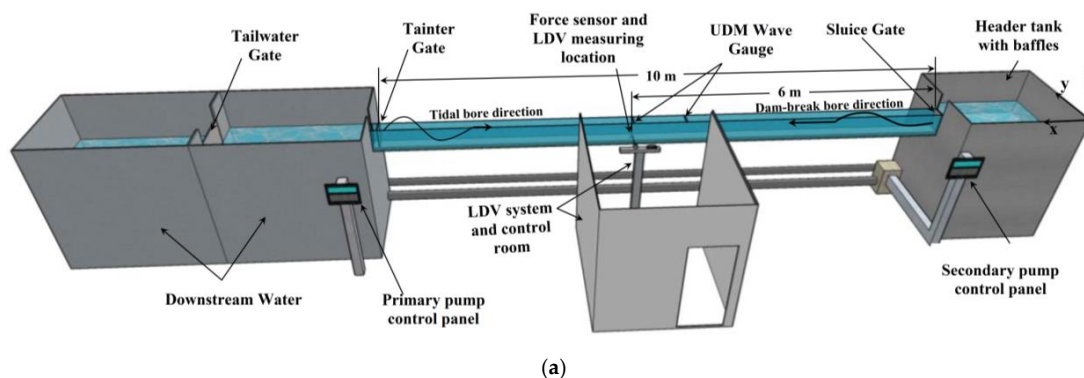


Figure 2. (a) Schematic diagram of the laboratory flume. (b) View of test section and installed bed.

Instantaneous velocity and turbulence were measured utilizing a dual-component laser Doppler anemometer (LDA), as illustrated in Figure 2. The velocity components and free surface measurements were simultaneously recorded along the channel centerline at $x = 6$ m. The LDA was positioned at various elevations above the rough bed, ranging from $5 < z < 101$ mm. A two-axis traverse system was employed to adjust and measure the vertical position z above the target particle. The downstream direction was denoted by positive V_x (longitudinal velocity), while positive V_z (vertical velocity) indicated upward movement, both perpendicular to the bed.

Throughout the experiments, velocity and force measurements were obtained at $x = 6$ m, while free water surface measurements were recorded at $x = 6$ and 6.5 m. A Zoom™ handy camera (60 fps) was utilized to capture video recordings between $x = 6$ and 7 m. To ensure data integrity, separate computers were employed for recording LDA data and force sensor and UDM data. The synchronization of all recordings was essential. The LDA system transmits an analog pulse signal to the NI-DAQ system to initiate the force sensor and UDM data collection. Manual synchronization of the camera with the LDA was achieved by introducing green light into the camera frame. All instruments were synchronized within ± 0.5 ms.

4. Experimental Results

4.1. Instantaneous Velocity and Free Surface Measurements

The data revealed consistent patterns across all flow conditions beneath the tidal bores. Figure 3 presents the median ensemble average (EA) velocity, water level, and forces component on top of the target particle for a range of Froude numbers ($Fr = 1.17$ – 1.45). A rapid deceleration in the longitudinal velocity component V_x was observed, accompanied by an initial acceleration and followed by a deceleration in the vertical velocity component V_z during bore passage. The longitudinal velocity (V_x) exhibits an abrupt decrease at $T \approx 500$, attributed to the impact of the breaking bore front (Figure 3a, $Fr = 1.45$), which generates turbulence and disrupts the flow around the particle. Subsequent to this initial reduction, V_x gradually increases, indicating the particle's acceleration as the effects of the bore dissipate. Concurrently, the vertical velocity (V_z) demonstrates a rapid increase, suggesting a strong upward force exerted by the bore, which is consistent with the elevated water depth observed during this phase. The substantial rise in water depth reflects a significant increase in the free surface due to the bore's momentum. Figure 3b ($Fr = 1.38$) presents a trend in V_x that indicates a less pronounced initial decrease compared to Figure 3a, suggesting that the breaking bore's impact is attenuated. This observation is corroborated by a more modest rise in V_z , indicating a reduced upward force acting on the particle. The changes in water depth also demonstrate a smaller increase than in Figure 3a, emphasizing the bore's diminished intensity at this Froude number. The initial deceleration of V_x is further reduced (Figure 3c), reflecting an even milder impact from the bore. Notably, V_z exhibits a less pronounced increase and may remain negative during certain phases, potentially indicating a more stable flow condition. A continued trend of oscillatory behaviour in V_x indicates weaker bores with less significant impacts on sediment transport (Figure 3d,e). The vertical velocity fluctuations become more pronounced, suggesting complex interactions between the particle and the flow, with minimal changes in water depth across both Froude numbers 1.21 and 1.17. The gradual decline in bore intensity is evident, highlighting the critical role that the Froude number plays in determining the dynamics of sediment transport and hydrodynamic forces.

Generally, a rapid deceleration in the longitudinal velocity component V_x was observed, accompanied by an initial acceleration followed by a deceleration in the vertical velocity component V_z during bore passage. The longitudinal velocity decreased significantly as the breaking bore advanced (Figure 3a–c), while the deceleration was less pronounced in the undular bore (Figure 3d,e). Upon the bore front's arrival at the sampling location ($x = 6$ m), a gradual increase in water depth occurred, resulting in a corresponding deceleration in V_x associated with a progressive rise in the free surface. A rapid reduction

in V_x coincided with a steep increase in the free surface. The vertical velocity V_z increased as the free surface increased but began to decelerate at the point of free surface curvature change, subsequently stabilizing at zero after the breaking bore passed (Figure 3a–c). For undular bores, both velocity components exhibited quasi-periodic fluctuations as wave undulations propagated through, with peak velocity values generally aligned with free surface elevation troughs, indicating an out-of-phase oscillation (Figure 3d,e).

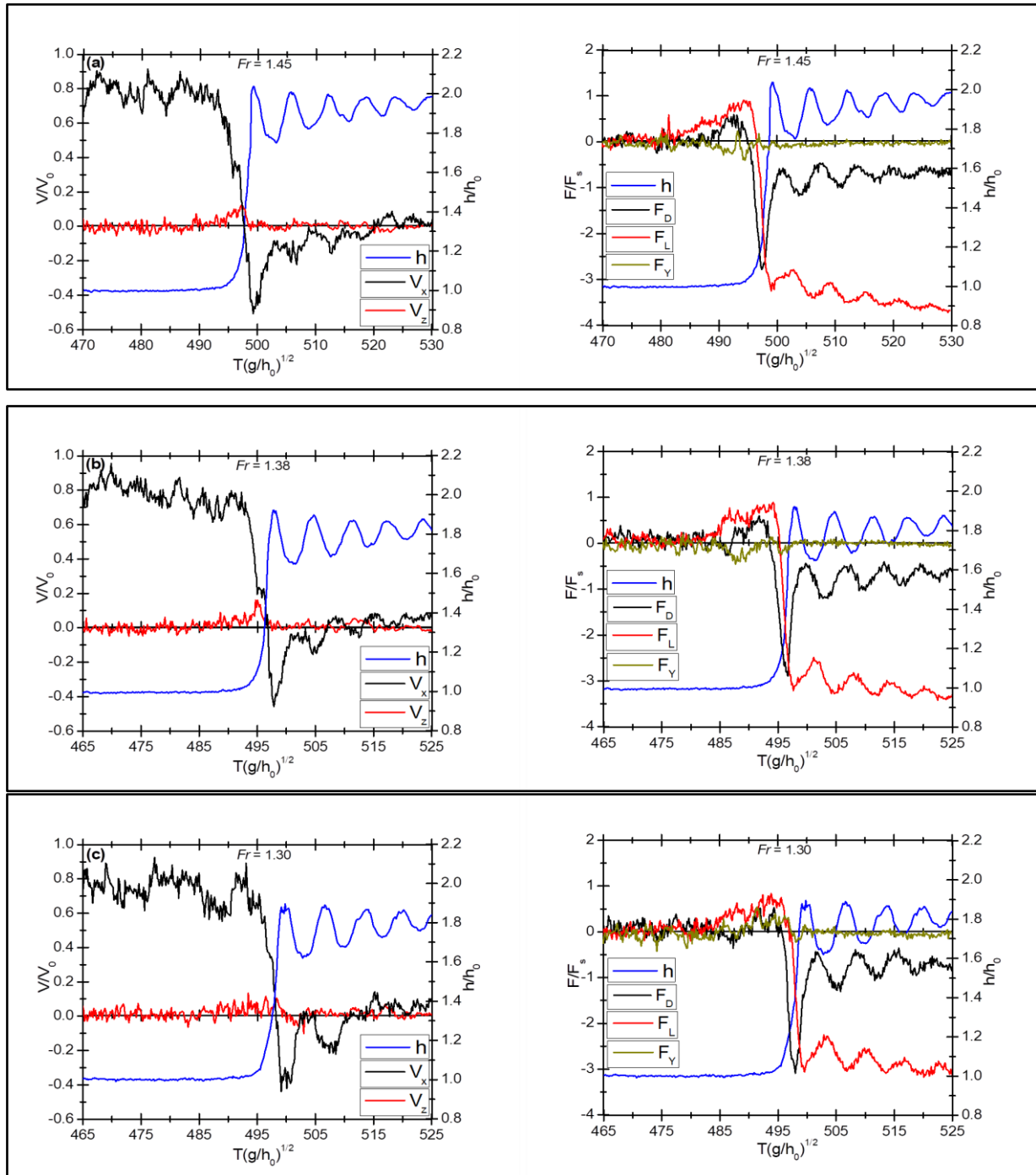


Figure 3. Cont.

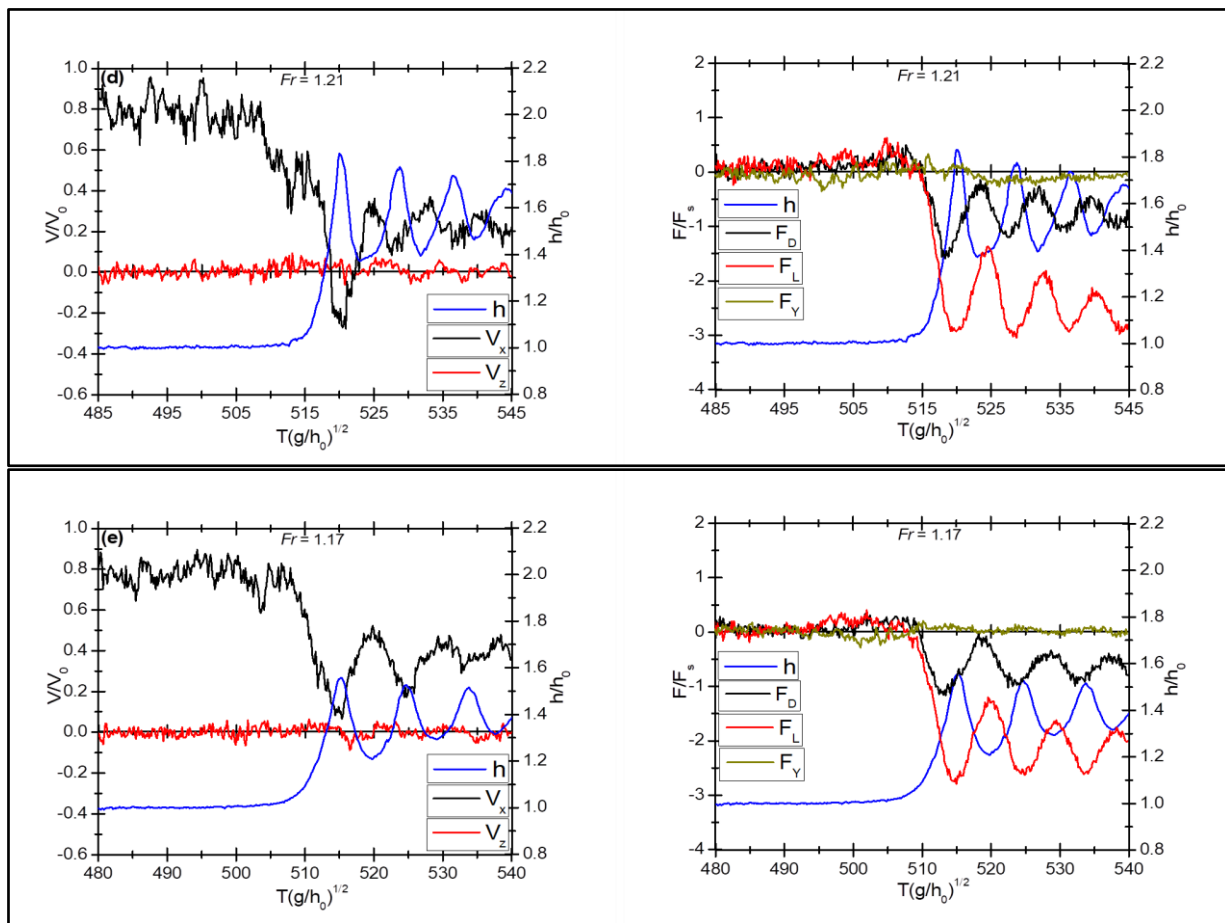


Figure 3. Median ensemble average forces, water depth, and velocity component at $x = 6$ m from the inlet tank and $z/h_0 = 0.037$ from the bed on top of the target particle. (a) For Froude number 1.45. (b) For Froude number 1.38. (c) For Froude number 1.30. (d) For Froude number 1.21. (e) For Froude number 1.17.

When the gate was fully closed, transient recirculation and negative longitudinal velocities, V_x , were observed near the channel invert during the breaking bore with secondary waves. In contrast, no negative longitudinal velocities were detected during the undular bore, as illustrated in Figure 3. This transient recirculation was observed for $z/h_0 < 0.39$ beyond the rough bed, beyond, which the longitudinal velocity component generally remained positive throughout the bore passage. Typically, this transient recirculation is observed in close proximity to the channel bed with $z/h_0 < 0.3\text{--}0.5$ [57]. These findings indicate an unsteady recirculation pattern associated with significant turbulent stresses in the water column, which potentially influences sediment processes in natural systems.

4.2. Sediment Motion and Forces on Target Particle

The instantaneous force components were recorded at $x = 6$ m from the upstream inlet of the channel for various Froude numbers under both the tidal and dam-break bores (Figure 2). Visual observations indicated that no pebble movement occurred prior to bore passage under steady flow conditions and constant static tailwater for both the tidal and dam-break bores. During the tidal undular bore, only a limited number of particles exhibited rotational movement from their initial positions. In contrast, under tidal-breaking and dam-break bore conditions, the majority of particle movements involved both rotation and translation. Additionally, minimal sediment saltation was observed near the bed beneath the tidal breaking bore, whereas significant sediment saltation was noted

as a consequence of the initial impact of dam-break bores. Overall, pebble motion was categorized into three basic modes based on visual analysis as shown in Figure 4:

- (1) Rotation in which the particle only changed its initial orientation without dislodgement mostly occurred in the undular and immediate before the arrival of the breaking bore, in both the upstream and downstream directions.
- (2) Rolling where the particle dislodged from its initial position as it continuously rolled over adjacent pebbles for a few particles in breaking and dam-break bores.
- (3) Saltating particle movement upstream along the breaking bore and downstream along the dam-break bore without touching the other pebbles.

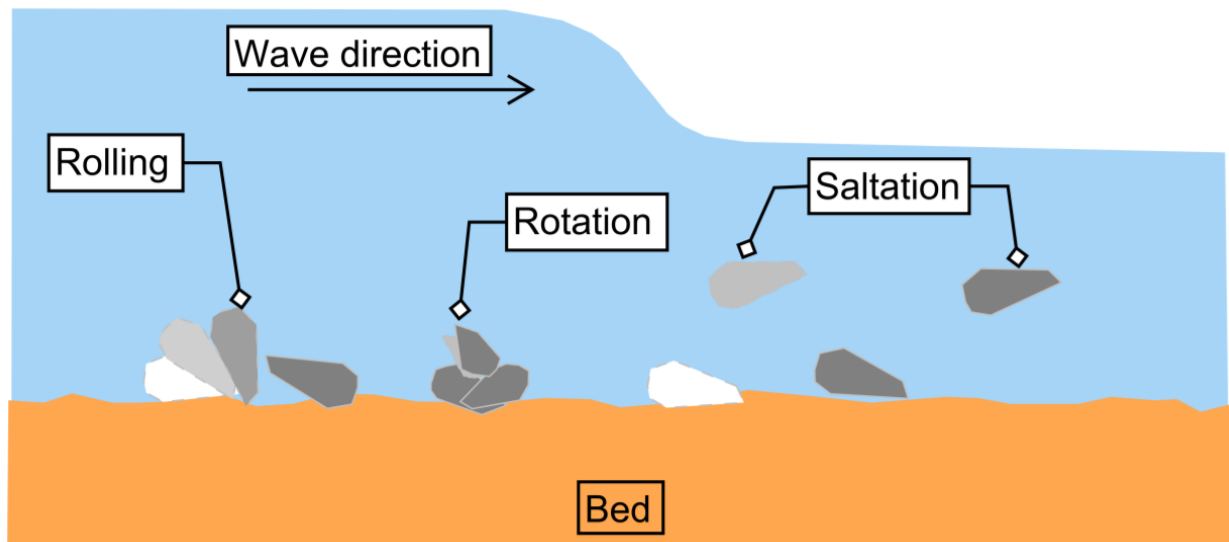


Figure 4. Modes of pebble motion.

During the tidal bore events, distinct sediment transport patterns were observed through visual assessment. Immediately prior to and concurrent with the passage of the roller toe, the pebbles predominantly exhibited upstream rolling and saltation. Conversely, downstream pebble rotation coincided with a gradual increase in water surface elevation. The majority of particles initiated upstream movement immediately following the passage of the roller toe. However, a small proportion of particles commenced downstream movement prior to the arrival of the roller toe. This feature was previously observed by [39], but they were unable to explain this phenomenon, which is well explained here based on the measured forces. However, during the passage of dam-break bores, visual observations demonstrated that the pebbles rolled and saltated downstream along the bore. The initial impact of the dam-break bore induced the majority of the pebbles to undergo displacement through rolling and saltation mechanisms.

4.2.1. Stages of Particle Motion Beneath Tidal Bore

Two distinct stages of particle motion were observed due to the continuous variation in forces for $Fr \geq 1.3 - 1.45$ (Figure 3a–c). Stage 1 encompassed the transition from the smooth rise of the free surface (point 1) to the roller toe (point 2), whereas Stage 2 extended from the roller toe to the peak of the first wave crest (point 3) (see Figures 2b and 5). In Stage 1, a limited number of particles exhibited rotation and rolling towards downstream, a phenomenon associated with an increase in upward vertical force F_v , which is correlated with a decelerating flow. During this stage, F_v was approximately 0.85 of the submerged weight of the target sphere utilized in this study. This upward vertical force generally reduces the friction between particles, thereby decreasing the intergranular force and resulting in minimal particle displacement.

In stage 2, a transient sheet flow occurred in the rolling and saltating modes towards upstream. The pebble upstream motion occurred due to the flow reversal, which gen-

erated a large drag force in the upstream direction, while F_v was still above 0.35 of the submerged weight.

Both drag and lift forces acted on the particle in the negative direction due to flow reversal from transient recirculation and the abrupt rise in the free water surface with the onset of the breaking bore. Consequently, the positive upward lift force plays a crucial role in saltation and facilitated pebble rolling. The peak force measurements generally corresponded to the troughs in the free surface elevation, indicating an out-of-phase oscillation (Figure 3). Furthermore, the lift and drag forces exhibit an out-of-phase relationship following the initial peak of the wave crest. Nearly all particles ceased motion when the maximum lift force was reached, approximately 0.4 s after the roller toe, while, during that period, the drag force began to increase in the positive direction. At that point, the lift force was negative (directed towards the bed) and was three times greater than the drag force, causing all particle movement to abruptly cease. This phenomenon was corroborated by visual observations.

Contrarily, for $Fr < 1.3 - 1.17$ (Figure 3d,e), only a few pebbles experienced rotation mode, where the pebble did not slide or roll over the surrounding contacting particles. They either retained the initial longitudinal orientation or changed the original orientation with less than one particle size movement. This motion was not a contribution to either the downstream or upstream sediment transport. At the arrival of the bore, around $T(g/h_0)^{0.5} \approx 515$ and 510 for Fr 1.21 and 1.17, respectively, Figure 3d,e showed that the drag and lift forces changed direction; however, the negative lift force is almost double compared to the drag force, which contributed to stabilising the particle. Directly measured force data also coincide with the visual observation. For these Froude numbers, measured forces have not shown significant positive upward F_v at the arrival of the bore (Figure 3d,e). However, beneath the initial peak of the wave crest, a negative downward lift force was observed to be twice the magnitude of the drag force. It is important to note that the restriction in particle movement was also influenced by the phase synchronization of drag and lift forces during the undular bore. Table 3 shows a comparison between F_v/F_s for undular and breaking bores.

Table 3. Comparison of the ratio of vertical to submerged force for undular and breaking bore.

Bore Type	Froude No.	F_v/F_s		Particle Movement Direction	
		Stage 1	Stage 2	Stage 1	Stage 2
Breaking	1.45	0.5 to 0.85	0.85 to -3.25	↑ & ↓	↑
Breaking	1.38	0.5 to 0.7	0.7 to -3.1	↑ & ↓	↑
Breaking	1.30	0.25 to 0.55	0.125	↑	↑
Undular	1.21	0 to -0.25	-0.25 to -2.9	-	-
Undular	1.17	0 to -0.15	-0.15 to -0.28	-	-

Notes: F_v , measured vertical force; F_s , submerged force of target sphere; ↓, downstream particle movement; ↑, upstream particle movement.

For all flow conditions, the transverse force exhibited significant fluctuations upon the arrival of the bore and subsequently diminished to near-zero levels after the first crest. The fluctuation is more pronounced for higher Froude numbers, as shown in Figure 3a–c, where the transverse force served as an additional facilitator for upstream pebble motion at the bore's arrival. The fluctuation is less pronounced for smaller Froude numbers (Figure 3d,e). The majority of particle entrainment events occurred within the region between the bore roller toe and the first crest.

4.2.2. Stages of Particle Motion Beneath Dam-Break Bore

Figure 5 illustrates the time-varying forces exerted on a target sphere during dam-break bore impacts for three different scenarios: weak, moderate, and strong bores. The diagram shows the stream-wise (F_D), lateral (F_Y), and vertical (F_L) force components. The

intensity of the bore, determined by its height and velocity, correlates positively with the magnitude of these forces, as shown in Figure 5a for weak, Figure 5b for moderate, and Figure 5c for strong bores, respectively. When the dam-break bore collides with the sphere, there is a swift increase in the longitudinal force, primarily due to the high-speed flow and the resulting hydrostatic pressure imbalance. During this initial impact, substantial sediment movement was observed, including pebbles rolling and bouncing along the bore, particularly during the strong bore (Figure 5c). The rapid increase in force occurred prior to the complete formation of quasi-steady forces, a phenomenon that transpired in less than one (1) second within the experimental context. Subsequent to the initial impact and full development of the bore flow, the horizontal forces gradually decreased, while the vertical force exhibited a sudden downward shift following its initial rise, as illustrated in Figure 5. The swift surge in horizontal force due to the initial impact, preceding the fully developed dam-break bore, emphasized the significance of the momentary uplift force in particle suspension (Figure 5c). This uplift force was found to diminish the effective stress, thereby promoting particle suspension in conjunction with the initial increase in horizontal force. A comparable effect was observed by Amicarelli et al. [50], who utilized three-dimensional numerical modelling to determine that sediment particles elevate around the dam-break front due to deviations in mean stress from equilibrium. Notably, as the bore height increased, fluctuations in both the horizontal and vertical hydrodynamic force magnitudes intensified following the initial bore impact.

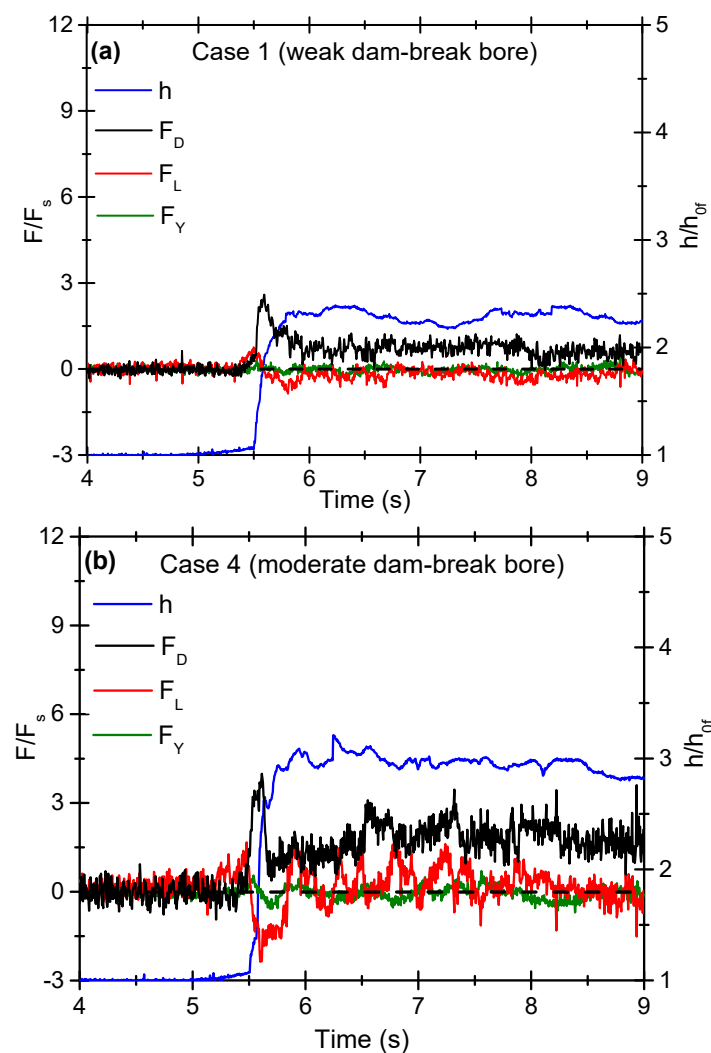


Figure 5. Cont.

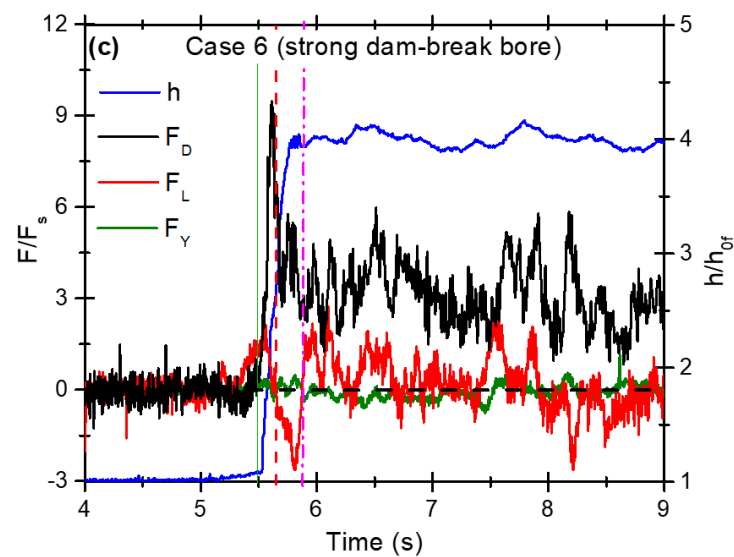


Figure 5. Median EA forces during dam-break bore with a constant Tailwater depth $h_{0f} \approx 37$ mm: (a) weak bore, (b) moderate bore, and (c) strong bore (Green to red line represents quadrant 1 and red to pink line represents quadrant 4 of measured forces during particle incipient motion).

The time series plots in Figure 5 demonstrate a gradual initial increase in the vertical uplift force applied to the target sphere as the bore approaches. This early rise is commonly referred to as a hydrodynamic uplift force [58]. Subsequently, the vertical force exhibits an abrupt decrease (toward the bed) until the peak water depth of the dam-break bore is attained; after which, it transitions into a quasi-steady hydrodynamic state. Once the dam-break bore was fully developed, pebble movement became negligible. The results indicate that, while the contribution of the lateral force increased with the strength of the dam-break bore, it remained comparatively insignificant relative to the horizontal and vertical forces.

4.3. Observational Verification of Vertical Force Effect on Incipient Motion

The directly measured data showed the importance of vertical force during the bore-induced sediment incipient motion. Figure 6 illustrates a representative example of the dynamic force patterns that occur during various phases of particle movement as tidal and dam-break bores progress. In the case of tidal bores, the initial phase is characterized by a gradual increase in the water surface elevation until it reaches the roller toe. The subsequent phase extends from the roller toe to the apex of the initial wave crest (for further details on these phases, refer to [29]). Recent investigations by Riaz et al. [29] revealed comparable trends, noting that the critical Shields number significantly deviates from Shields' original prediction. They posited that this variation is attributable to the oscillating forces present during different stages of the tidal bore, resulting in a variable critical Shields parameter rather than a constant value.

This can be further clarified by dividing the measured forces into four quadrants: quadrant 1 (Q1) with positive downstream shear (longitudinal) and vertical upward (normal to bed) force, Q2 with positive upward vertical force and negative (towards upstream) shear force, Q3 with negative (towards bed) vertical force and negative (upstream) shear force, and Q4 with positive shear force and negative vertical force.

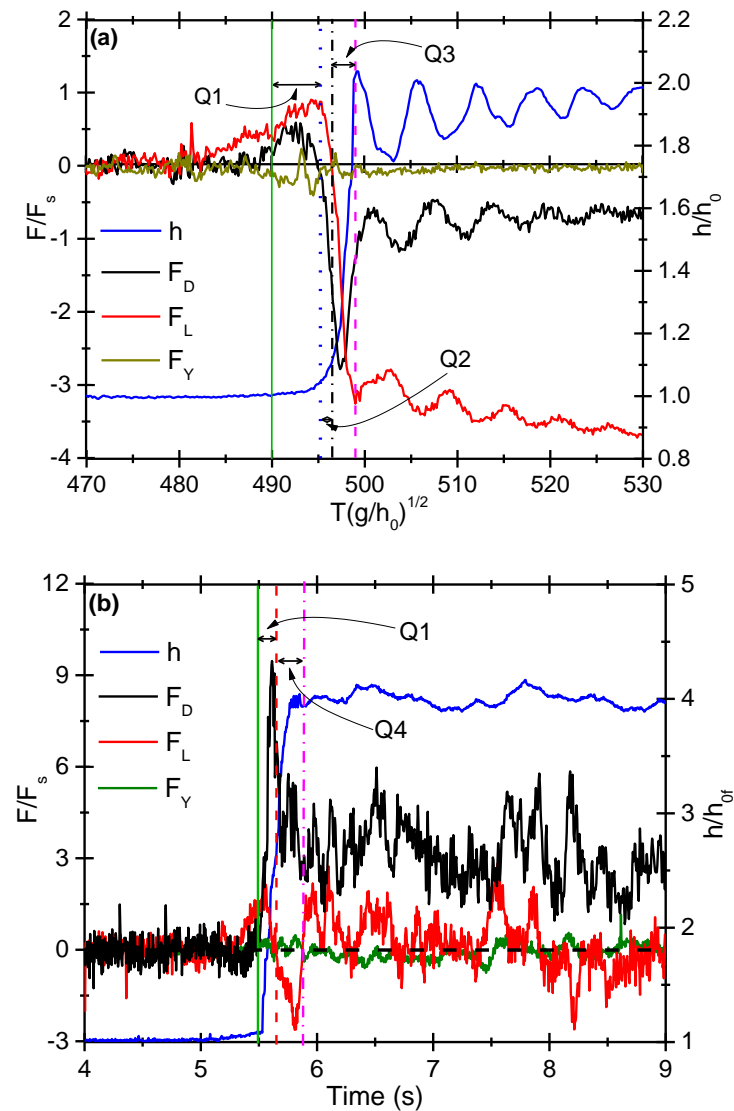


Figure 6. Median EA water depth and force component. (a) Tidal breaking bore. (b) Dam-break bore for all stages of particle movement. Q1, Q2, Q3, and Q4 represent the quadrant of measured forces during particle incipient motion.

A comparison of Equation (13) with directly measured forces is shown in Figure 7, which shows a plot $\tau'_{c(y)}/\tau_{c(0)}$ versus F_v/F_s , where $\tau'_{c(y)}$ and $\tau_{c(0)}$ is critical shear stress with and without vertical force, and F_v and F_s are the measured vertical force and submerged force, respectively. Force measurements during tidal and dam-break bores revealed that the forces could be categorized into four distinct quadrants, each representing different stages of initial sediment movement. The early phase of tidal bores exhibited an increasing trend in both horizontal and vertical forces. This phenomenon was particularly evident in tidal breaking bores with bubbles, which facilitated downstream particle movement and reduced pebble stability. As the tidal bore approached the measurement site, the water level began to rise, resulting in upward forces recorded between $490 < T(g/h_0)^{0.5} < 495.5$ (Figure 6). This vertical force induced downstream movement in some pebbles. During this period, measured forces showed that forces fall in the first quadrant (Q1), where both vertical and horizontal forces were positive upward and along the initial flow, respectively. One can infer from Figure 6 that, when the lift to submerged force ratio is higher, a small shear force is enough to move the particle in the downstream direction, whereas more longitudinal force will be required when the ratio of lift to submerged force is smaller. It is

essential to emphasize that the primary factor driving particle movement is the enhanced lift force rather than the increased shear stress.

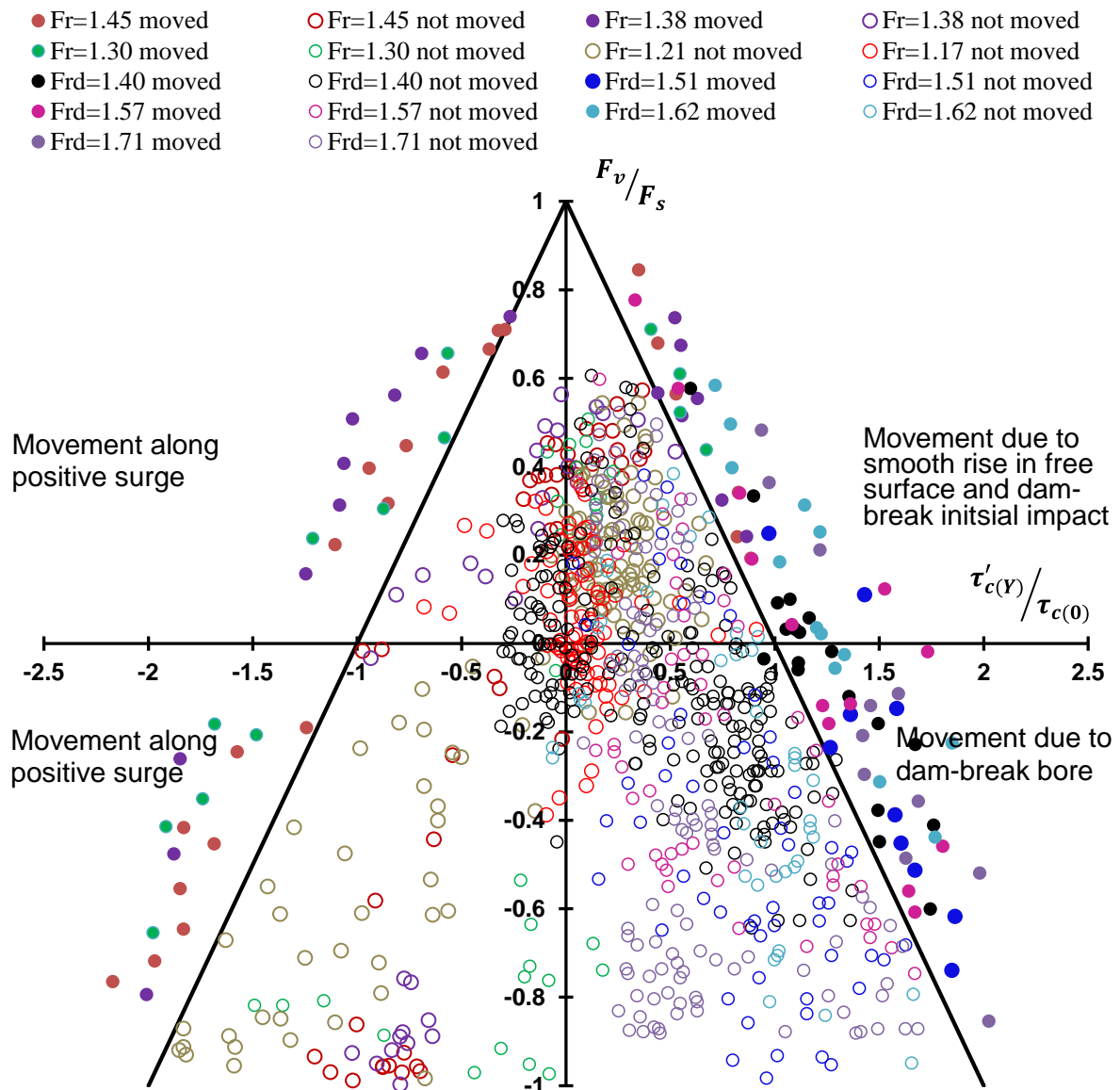


Figure 7. Prism diagram of experimental and predicted critical shear stress subject to vertical force due to a wave. Open circles indicate no particle movement; filled circles indicate particle movement. Fr and Fr_d represents Froude numbers of the tidal bore and dam-break bore, respectively.

During the tidal bore’s second stage, the upward force began to decrease, while the drag force experienced a significant reduction. As the flow direction changed, the vertical force became crucial in initiating particle motion. During the period of $495.5 < T(g/h_0)^{0.5} < 497$ (Figure 5), the bore transported pebbles upstream, and the recorded data indicated that forces were positioned in the second quadrant (Q2). With time, F_v becomes zero and the drag force is double the submerged force, which is enough for pebbles movement along the bore. During stage 2 when the F_v changed the direction downward into the bed, particles were still moving upstream in the third quadrant (Q3). When the particles experienced the maximum negative vertical force beneath the apex of the initial wave crest, they ceased motion instantaneously.

During the dam-break bores, all the observed particle moved along the bore. At the initial impact of dam-break bore, both horizontal and vertical forces were positive and falls in first quadrant (Q1). After the initial impact of dam-break bore, the F_v changed the

direction downward into the bed, while the drag force was almost at its peak and particles were moved downstream along the bore. The measured data showed that forces fall in the fourth quadrant (Q4). The initiation of particle movement was significantly influenced by drag force at the critical moment. From the current experiments, more than 300 particles were analysed during tidal and dam-break bores. From Figure 7, it can be concluded that a minimal value of $F = F_v/F_s$ can substantially influence the critical shear stress.

5. Discussion on Forces Induced by Unsteadiness and Its Effects

Sediment transport in rivers and oceans is significantly influenced by the dynamic nature of flow, particularly during flood or tidal events. Equations derived from steady-state conditions often prove inadequate when applied to unsteady flows, resulting in diminished accuracy. Research, including studies by Graf [59], has consistently demonstrated that the actual rate of sediment transport in unsteady flows exceeds the predictions made using these equations. This paper considers why the observed critical threshold condition of sediment transport is not valid in spatially varied flows. Furthermore, the investigation demonstrates that the vertical force exerts a significant influence on constraining the applicability of the Shields curve. Typically, drag and lift forces are calculated using the formulas $F_D = 0.5 \cdot C_D \cdot \rho_w \cdot A \cdot V_x^2$ and $F_v = 0.5 \cdot C_L \cdot \rho_w \cdot A \cdot V_x^2$, respectively, where V_x is the streamwise velocity, A is the cross-sectional area of the particle facing the flow, and C_D and C_L are the drag and lift coefficients, respectively. Research by Yang [32] and Lamb et al. [37] demonstrated that vertical forces can originate from sources beyond groundwater seepage, including the non-uniformity and unsteadiness of the primary flow. These forces can exert either upward or downward pressure, independent of the streamwise velocity V_x . These findings challenge conventional sediment transport theory, which posits that lift force is exclusively generated by longitudinal velocity, invariably acting upward, and only ceases when the longitudinal velocity reaches zero.

Under natural conditions, surface and subsurface waters interact, meaning that F is always non-zero (i.e., $F \neq 0$). This interaction creates a discrepancy when comparing the Shields curve with field data. This investigation demonstrated that the critical Shields parameter exhibited multiple values for a single D_* (specifically, 444 and 109), where D_* represents the dimensionless particle diameter of the target sphere. Figure 8 illustrates the pebbles with d_{50} measurements of 36.6 mm and 4 mm, respectively, and compares them to previously published findings [7,60–65]. The results indicate that the observed critical Shields number significantly deviates from Shields' prediction, represented by the solid line. The lines in Figure 8 are results calculated using different values of F in Equation (13) (where $F = F_v/F_s = 0$). We attribute the non-unique values of the critical Shields parameter to the varying forces at different stages of tidal and dam-break bores. At the initial impact of the bore, shear stress was reduced due to upward motion (i.e., positive vertical force), causing the pebbles to move below the critical Shields threshold ($\tau_{*c} = 0.045$), thereby increasing particle mobility. This finding aligns with Yang's [32] results and indicates that pebble incipient motion was driven by decreasing pressure gradients and an increasing trend in uplift force.

Classic theory posits that drag force is invariably proportional to the square of velocity, and lift force consistently acts in an upward direction. However, recent investigations challenge this assumption, demonstrating that, while drag force is associated with near-bed velocity, it does not always exhibit a squared relationship with streamwise velocity. In tidal bore breaking rollers, when V_x reached its minimum, F_D was observed to be twice the value of F_v , with F_v approaching zero. Furthermore, numerous particles were observed moving upstream along the bore due to drag force, suggesting that this force was likely induced by a steep pressure gradient rather than longitudinal velocity [14,18,27,37]. Furthermore, direct measurements revealed a significant downward F_v trend subsequent to the roller toe, presumably attributable to the pressure gradient. The increased negative or downward vertical force during the breaking roller enhanced particle stability, thereby impeding movement [32]. Nevertheless, sediment transport persisted if the drag force (F_D) attained a

sufficient magnitude. This observation aligns with previous research [32,37,66,67], indicating that drag force constituted the primary factor driving upstream pebble movement during the breaking roller stage. After the first peak of the wave crest in the tidal bore, pebble movement suddenly ceased, despite shear stress exceeding $\tau_{*c} = 0.045$, suggesting that the increased downward lift force likely stabilized the particles. Our investigation demonstrates that lateral force exerts a significant influence on sediment transport, even in the presence of opposing gravitational forces. Consequently, direct force measurements indicate that both longitudinal and perpendicular forces are fundamental to sediment transportation.

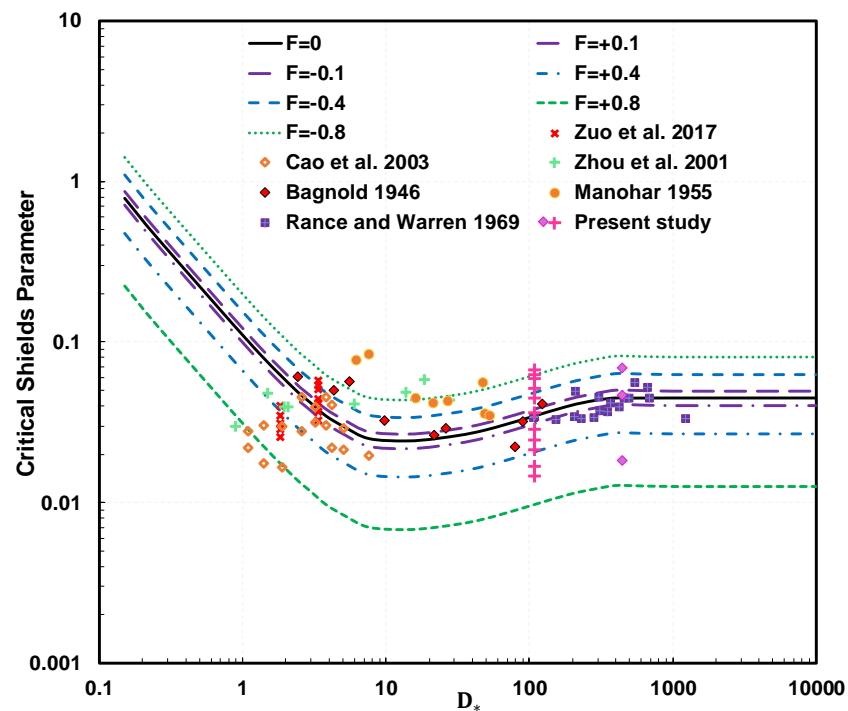


Figure 8. Influence of vertical force on critical shear stress; the solid line is the original Shields curve (or $F = 0$), and the other lines are calculated from Equation (13) with different F [60–65].

An investigation into shear stress and the Shields parameter revealed that the highest critical Shields parameter was below 0.02. Classic theories suggest that sediment transport should not occur at such low values. Nevertheless, the research found that sediment movement was possible when upward velocity was present, a phenomenon Yang [32] termed the “lightened particles” effect. This finding indicates that the uplift force must be taken into account when studying sediment incipient motion. The fluctuating nature of the vertical force challenges the applicability of the Shields curve, as its direction can change. Studies by Yang [32] and Francalanci et al. [30] also highlighted the significance of the vertical component and the non-hydrostatic vertical pressure gradient within the sediment layer in determining the limitations of the Shields parameter. Figure 8 illustrates Shields curves as parallel lines representing different F values derived from Equation (13). The significant discrepancies observed between the measured critical shear stress and Shields’ predictions can be attributed to the non-zero F values. These values account for the deviation of data points from the original Shields curve ($F = 0$), where F is equivalent to 0.

This study presents a theoretical framework supported by empirical measurements of fluid dynamic forces during a positive surge. The findings provide quantitative insight into the initiation, force, and velocity of sediment transport in tidal bores, potentially elucidating the substantial sediment suspension and bed load phenomena observed in previous research. Future investigations should focus on establishing a correlation between these forces and a readily measurable field parameter, such as the velocity of wave orbitals.

6. Conclusions

This study examines the limitations of current sediment transport models in accurately predicting the initiation, entrainment, and movement of particles. This study posits that the inadequacies in existing sediment transport equations can be attributed to multiple factors, with particular emphasis on the absence of a vertical force component. It is hypothesized that this vertical force, operating in conjunction with streamwise variables, is critical for determining the onset of the sediment motion. The incorporation of the vertical force into these equations could provide a more comprehensive explanation of the various phenomena observed in both laboratory and field studies. The significance of the vertical movement should not be underestimated. The research concludes with the following observations:

Sediment mobility is enhanced by an upward vertical force, while a downward force into the bed increases its stability. The concept of apparent density can be utilized to mathematically represent the influence of vertical force on sediment transport. Sediment experiencing a downward force with a negative vertical component exhibited increased apparent density, whereas an upward vertical force results in decreased apparent density. The critical shear stress necessary for sediment transport is also affected by vertical force, with an upward force reducing it and downward force increasing it. To account for the critical shear stress in highly unsteady flows, the Shields curve can be extended by incorporating the concept of the apparent sediment density.

This investigation establishes a foundation for more accurate predictions of sediment incipient motion during tidal and dam-break bore propagation, potentially resulting in significant improvements in hydro-sediment modeling frameworks. These enhancements are crucial for improving the coastal and river management practices. Further research should investigate the effects of positive surges on bathymetry changes and examine how artificial intelligence technologies can be employed to address sediment transport challenges more efficiently and precisely.

Author Contributions: Conceptualization, M.Z.B.R., U.I., S.-Q.Y., M.S. and M.N.A.; Methodology, M.Z.B.R., H.Z., S.-Q.Y., M.S., R.J. and M.N.A.; Formal analysis, M.Z.B.R., U.I. and M.N.A.; Investigation, M.Z.B.R.; Data curation, M.Z.B.R. and H.Z.; Writing—original draft, M.Z.B.R.; Writing—review & editing, M.Z.B.R., U.I., H.Z., S.-Q.Y., M.S., R.J. and M.N.A.; Visualization, M.Z.B.R.; Supervision, S.-Q.Y. and M.S. All authors have read and agreed to the published version of the manuscript.

Funding: This research received no external funding.

Data Availability Statement: The data can be provided on demand.

Conflicts of Interest: The authors declare no conflicts of interest.

References

1. Zhang, M.; Yu, G. Critical conditions of incipient motion of cohesive sediments. *Water Resour. Res.* **2017**, *53*, 7798–7815. [[CrossRef](#)]
2. Ribberink, J.S.; Al-Salem, A.A. Sediment transport in oscillatory boundary layers in cases of rippled beds and sheet flow. *J. Geophys. Res. Ocean.* **1994**, *99*, 12707–12727. [[CrossRef](#)]
3. Voropayev, S.; Roney, J.; Boyer, D.; Fernando, H.; Houston, W. The motion of large bottom particles (cobbles) in a wave-induced oscillatory flow. *Coast. Eng.* **1998**, *34*, 197–219. [[CrossRef](#)]
4. Yamaguchi, N.; Sekiguchi, H. Effect of velocity hiatuses in oscillatory flow on migration and geometry of ripples: Wave-flume experiments. *Sedimentology* **2010**, *57*, 720–733. [[CrossRef](#)]
5. Moulton, M.; Elgar, S.; Raubenheimer, B. A surfzone morphological diffusivity estimated from the evolution of excavated holes. *Geophys. Res. Lett.* **2014**, *41*, 4628–4636. [[CrossRef](#)]
6. Riaz, M.Z.B.; Ly, K.L. The investigation of Nature-based Solutions (NbSs) as local scour countermeasures around bridge piers: A numerical study. In *HWRS2023: Hydrology & Water Resources Symposium*; Engineers Australia: Sydney, Australia, 2023; pp. 881–891.
7. Shields, A. *Application of Similarity Principles and Turbulence Research to Bed-Load Movement*; California Institute of Technology: Pasadena, CA, USA, 1936.
8. Grant, W.D.; Madsen, O.S. Combined wave and current interaction with a rough bottom. *J. Geophys. Res. Ocean.* **1979**, *84*, 1797–1808. [[CrossRef](#)]

9. Madsen, O.S.; Wikramanayake, P.N. Simple Models for Turbulent Wave-Current Bottom Boundary Layer Flow; Massachusetts Inst of Tech Cambridge Ralph M Parsons Lab for Water Resources. 1991. Available online: <https://ui.adsabs.harvard.edu/abs/1991STIN...9232630M> (accessed on 5 October 2024).
10. Styles, R.; Glenn, S.M. Modeling stratified wave and current bottom boundary layers on the continental shelf. *J. Geophys. Res. Ocean.* **2000**, *105*, 24119–24139. [[CrossRef](#)]
11. Lin, P.; Liu, P.L.F. Turbulence transport, vorticity dynamics, and solute mixing under plunging breaking waves in surf zone. *J. Geophys. Res. Ocean.* **1998**, *103*, 15677–15694. [[CrossRef](#)]
12. Lin, P.; Liu, P.L.-F. A numerical study of breaking waves in the surf zone. *J. Fluid Mech.* **1998**, *359*, 239–264. [[CrossRef](#)]
13. Afzalimhr, H.; Dey, S.; Rasoulifar, P. Influence of decelerating flow on incipient motion of a gravel-bed stream. *Sadhana* **2007**, *32*, 545–559. [[CrossRef](#)]
14. Frank, D.; Foster, D.; Sou, I.M.; Calantoni, J.; Chou, P. Lagrangian measurements of incipient motion in oscillatory flows. *J. Geophys. Res. Ocean.* **2015**, *120*, 244–256. [[CrossRef](#)]
15. Riaz, M.Z.B.; Yang, S.-Q.; Sivakumar, M. Laboratory measurements of velocity and hydrodynamic force over coarse fixed rough bed. In *ICHWR; CEWRE: Lahore, Pakistan*, 2021.
16. Riaz, M.Z.B.; Yang, S.-Q.; Sivakumar, M. Hydrodynamic Forces Generated on a Coarse Spherical Particle Beneath a Tidal Bore. In *Webinar on Experimental Methods and Laboratory Instrumentation in Hydraulics*; InstGeoph_PAS_Publs: Warszawa, Poland, 2021. Available online: <https://pub.igf.edu.pl/book-of-extended-abstracts-webinar-on-experimental-methods-and-laboratory-instrumentation-in-hydraulics-13-15-april-2021,4,en,pubs,4,0,5,152.html> (accessed on 5 October 2024).
17. Riaz, M.Z.B. Role of Hydrodynamic Forces on Incipient Motion of Sediment in Unsteady Flows. Ph.D. Thesis, University of Wollongong, Wollongong, Australia, 2022.
18. Foster, D.; Bowen, A.; Holman, R.A.; Natto, P. Field evidence of pressure gradient induced incipient motion. *J. Geophys. Res. Ocean.* **2006**, *111*, C05004. [[CrossRef](#)]
19. Buffington, J.M.; Montgomery, D.R. A systematic analysis of eight decades of incipient motion studies, with special reference to gravel-bedded rivers. *Water Resour. Res.* **1997**, *33*, 1993–2029. [[CrossRef](#)]
20. Lamb, M.P.; Dietrich, W.E.; Venditti, J.G. Is the critical Shields stress for incipient sediment motion dependent on channel-bed slope? *J. Geophys. Res. Earth Surf.* **2008**, *113*, F02008. [[CrossRef](#)]
21. Grabowski, R.C.; Droppo, I.G.; Wharton, G. Erodibility of cohesive sediment: The importance of sediment properties. *Earth-Sci. Rev.* **2011**, *105*, 101–120. [[CrossRef](#)]
22. Aksoy, H.; Mohammadi, M. Artificial neural network and regression models for flow velocity at sediment incipient deposition. *J. Hydrol.* **2016**, *541*, 1420–1429.
23. Calantoni, J.; Puleo, J.A. Role of pressure gradients in sheet flow of coarse sediments under sawtooth waves. *J. Geophys. Res. Ocean.* **2006**, *111*, C01010. [[CrossRef](#)]
24. Madsen, O.S. Stability of a sand bed under breaking waves. In *Coastal Engineering 1974*; American Society of Civil Engineers: Reston, VA, USA, 1975; pp. 776–794.
25. Sleath, J.F. Conditions for plug formation in oscillatory flow. *Cont. Shelf Res.* **1999**, *19*, 1643–1664. [[CrossRef](#)]
26. Nielsen, P. Shear stress and sediment transport calculations for swash zone modelling. *Coast. Eng.* **2002**, *45*, 53–60. [[CrossRef](#)]
27. Terrile, E.; Reniers, A.J.; Stive, M.J.; Tromp, M.; Verhagen, H.J. Incipient motion of coarse particles under regular shoaling waves. *Coast. Eng.* **2006**, *53*, 81–92. [[CrossRef](#)]
28. Myrhaug, D.; Slaattelid, O.; Soulsby, R.; Lambrakos, K. Measurements and analysis of flow velocity and sediment concentration at the seabed. *Appl. Mech. Rev.* **1995**, *48*, 570–588. [[CrossRef](#)]
29. Riaz, M.Z.B.; Yang, S.Q.; Sivakumar, M.; Enever, K.; Miguntanna, N.S.; Khalil, U. Direct measurements of hydrodynamic forces induced by tidal bores. *Water Resour. Res.* **2021**, *57*, e2020WR028970. [[CrossRef](#)]
30. Francalanci, S.; Parker, G.; Solari, L. Effect of seepage-induced nonhydrostatic pressure distribution on bed-load transport and bed morphodynamics. *J. Hydraul. Eng.* **2008**, *134*, 378–389. [[CrossRef](#)]
31. Berni, C.; Michallet, H.; Barthélemy, E. Effects of horizontal pressure gradients on bed destabilization under waves. *J. Fluid Mech.* **2017**, *812*, 721–751. [[CrossRef](#)]
32. Yang, S.-Q. Formula for Sediment Transport Subject to Vertical Flows. *J. Hydraul. Eng.* **2019**, *145*, 04019013. [[CrossRef](#)]
33. Riaz, M.; Yang, S.; Sivakumar, M. *Simultaneous Measurement of Horizontal and Vertical Velocities and Forces Beneath a Tidal Bore*, *Coastlab20*; IAHR: Zhoushan, China, 2020; p. 8.
34. Papanicolaou, A.; Diplas, P.; Evaggelopoulos, N.; Fotopoulos, S. Stochastic incipient motion criterion for spheres under various bed packing conditions. *J. Hydraul. Eng.* **2002**, *128*, 369–380. [[CrossRef](#)]
35. Liu, P.L.; Park, Y.S.; Lara, J.L. Long-wave-induced flows in an unsaturated permeable seabed. *J. Fluid Mech.* **2007**, *586*, 323–345. [[CrossRef](#)]
36. Scholtès, L.; Chareyre, B.; Michallet, H.; Catalano, E.; Marzougui, D. Modeling wave-induced pore pressure and effective stress in a granular seabed. *Contin. Mech. Thermodyn.* **2015**, *27*, 305–323. [[CrossRef](#)]
37. Lamb, M.P.; Brun, F.; Fuller, B.M. Direct measurements of lift and drag on shallowly submerged cobbles in steep streams: Implications for flow resistance and sediment transport. *Water Resour. Res.* **2017**, *53*, 7607–7629. [[CrossRef](#)]
38. Guo, J. Empirical Model for Shields Diagram and Its Applications. *J. Hydraul. Eng.* **2020**, *146*, 04020038. [[CrossRef](#)]

39. Khezri, N.; Chanson, H. Turbulent velocity, sediment motion and particle trajectories under breaking tidal bores: Simultaneous physical measurements. *Environ. Fluid Mech.* **2015**, *15*, 633–650. [[CrossRef](#)]
40. Einstein, H.A.; El-Samri, E.-S.A. Hydrodynamic forces on a rough wall. *Rev. Mod. Phys.* **1949**, *21*, 520. [[CrossRef](#)]
41. Schmeeckle, M.W.; Nelson, J.M.; Shreve, R.L. Forces on stationary particles in near-bed turbulent flows. *J. Geophys. Res. Part F Earth Surf.* **2007**, *112*, 1–21. [[CrossRef](#)]
42. Dwivedi, A.; Melville, B.; Raudkivi, A.J.; Shamseldin, A.Y.; Chiew, Y.-M. Role of turbulence and particle exposure on entrainment of large spherical particles in flows with low relative submergence. *J. Hydraul. Eng.* **2012**, *138*, 1022–1030. [[CrossRef](#)]
43. Wei, Z.; Dalrymple, R.A.; Hérault, A.; Bilotta, G.; Rustico, E.; Yeh, H. SPH modeling of dynamic impact of tsunami bore on bridge piers. *Coast. Eng.* **2015**, *104*, 26–42. [[CrossRef](#)]
44. Xu, Z.; Melville, B.; Whittaker, C.; Nandasena, N.; Shamseldin, A. Mitigation of tsunami bore impact on a vertical wall behind a barrier. *Coast. Eng.* **2021**, *164*, 103833. [[CrossRef](#)]
45. Shafiei, S.; Melville, B.W.; Shamseldin, A.Y. Experimental investigation of tsunami bore impact force and pressure on a square prism. *Coast. Eng.* **2016**, *110*, 1–16. [[CrossRef](#)]
46. Chuang, W.-L.; Chang, K.-A.; Kaihatu, J.; Cienfuegos, R.; Mokrani, C. Experimental study of force, pressure, and fluid velocity on a simplified coastal building under tsunami bore impact. *Nat. Hazards* **2020**, *103*, 1093–1120. [[CrossRef](#)]
47. Kikkert, G.A.; O'Donoghue, T.; Pokrajac, D.; Dodd, N. Experimental study of bore-driven swash hydrodynamics on impermeable rough slopes. *Coast. Eng.* **2012**, *60*, 149–166. [[CrossRef](#)]
48. Alexander, J.; Cooker, M.J. Moving boulders in flash floods and estimating flow conditions using boulders in ancient deposits. *Sedimentology* **2016**, *63*, 1582–1595. [[CrossRef](#)]
49. Liu, X.; Infante Sedano, J.Á.; Mohammadian, A. A coupled two-dimensional numerical model for rapidly varying flow, sediment transport and bed morphology. *J. Hydraul. Res.* **2015**, *53*, 609–621. [[CrossRef](#)]
50. Amicarelli, A.; Kocak, B.; Sibilla, S.; Grabe, J. A 3D smoothed particle hydrodynamics model for erosional dam-break floods. *Int. J. Comput. Fluid Dyn.* **2017**, *31*, 413–434. [[CrossRef](#)]
51. Xu, B.; Zhang, S.; Nielsen, P.; Wüthrich, D. Measurements of bed shear stresses near the tip of dam-break waves on a rough bed. *Exp. Fluids* **2021**, *62*, 49. [[CrossRef](#)]
52. Yang, S. *Influence of Vertical Velocity on Sediment Transport*; IAHR-APD: Jeju Island, Republic of Korea, 2012.
53. Cheng, N.-S.; Chiew, Y.-M. Incipient sediment motion with upward seepage. *J. Hydraul. Res.* **1999**, *37*, 665–681. [[CrossRef](#)]
54. Schlichting, H.; Kestin, J.; Street, R.L. Boundary-Layer Theory (Seventh Edition). *J. Fluids Eng.* **1980**, *102*, 125. [[CrossRef](#)]
55. Julien, P.Y. *Erosion and Sedimentation*; Cambridge University Press: Cambridge, UK, 1994.
56. Farvizi, F.; Melville, B.W.; Shamseldin, A.Y.; Shafiei, S.; Hendi, E. Experimental investigation of tsunami bore-induced forces and pressures on skewed box section bridges. *Ocean Eng.* **2021**, *224*, 108730. [[CrossRef](#)]
57. Chanson, H.; Toi, Y.-H. Physical modelling of breaking tidal bores: Comparison with prototype data. *J. Hydraul. Res.* **2015**, *53*, 264–273. [[CrossRef](#)]
58. Livermore, S.N. Evaluation of Tsunami Design Codes and Recommendations for Bridges Susceptible to Tsunami Inundation. Master's Thesis, University of Washington, Seattle, WA, USA, 2014.
59. Graf, W.H. Sediment transport in steep channel. *J. Hydrosoci. Hydr. Eng. JSCE* **1987**, *5*, 11–26.
60. Bagnold, R.A. Motion of waves in shallow water. Interaction between waves and sand bottoms. *Proc. R. Soc. London. Ser. A Math. Phys. Sci.* **1946**, *187*, 1–18.
61. Manohar, M. *Mechanics of Bottom Sediment Movement Due to Wave Action*; Tech. Memo. 75. Beach Erosion Board; U.S. Army Corps of Engineers: Washington, DC, USA, 1955.
62. Rance, P.; Warren, N. The threshold of movement of coarse material in oscillatory flow. In *Coastal Engineering 1968*; American Society of Civil Engineers: Reston, VA, USA, 1969; pp. 487–491.
63. Zhou, Y.; Chen, Y.; Ma, Q. Threshold of sediment movement in different wave boundary layers. *China Ocean Eng.* **2001**, *15*, 509–520.
64. Zuo, L.; Roelvink, D.; Lu, Y.; Li, S. On incipient motion of silt-sand under combined action of waves and currents. *Appl. Ocean. Res.* **2017**, *69*, 116–125. [[CrossRef](#)]
65. Cao, Z.; Kong, L.; Jiao, G. Sediment incipient motion under co-action of waves and currents. *Acta Oceanol. Sin.* **2003**, *25*, 113–119.
66. Hassan, M.A.; Egozi, R.; Parker, G. Experiments on the effect of hydrograph characteristics on vertical grain sorting in gravel bed rivers. *Water Resour. Res.* **2006**, *42*, W09408. [[CrossRef](#)]
67. Emadzadeh, A.; Chiew, Y.M.; Afzalimehr, H. Effect of accelerating and decelerating flows on incipient motion in sand bed streams. *Adv. Water Resour.* **2010**, *33*, 1094–1104. [[CrossRef](#)]

Disclaimer/Publisher's Note: The statements, opinions and data contained in all publications are solely those of the individual author(s) and contributor(s) and not of MDPI and/or the editor(s). MDPI and/or the editor(s) disclaim responsibility for any injury to people or property resulting from any ideas, methods, instructions or products referred to in the content.